
Article:
Onodera, Yuta, Elphick, Kelvin, Kanemura, Takuro et al. (8 more authors) (2020) Experimental inspection of a computationally-designed NiCrMnSi Heusler alloy with high Curie temperature. Japanese Journal of Applied Physics. pp. 1-6. ISSN: 1347-4065

https://doi.org/10.35848/1347-4065/ab9c75

Experimental inspection of a computationally-designed NiCrMnSi Heusler alloy with high Curie temperature

Y. Onodera[1,2], K. Elphick[3], T. Kanemura[4], T. Roy[4], T. Tsuchiya[5,6], M. Tsujikawa[4,6], K. Yoshida[7], Y. Nagai[7], S. Mizukami[2,6,5]*, A. Hirohata[3], M. Shirai[4,6,5],

[1]*Department of Applied Physics, Tohoku Univ., Aoba 6-6-05, Sendai 980-8579, Japan* [2]*WPI Advanced Institute for Material Research, Tohoku Univ., Katahira 2-1-1, Sendai 980-8577, Japan* [3]*Department of Electronic Engineering, University of York, York YO10 5DD, United Kingdom* [4]*Research Institute of Electrical Communication (RIEC), Tohoku University, Sendai 980-8579, Japan* [5]*Center for Science and Innovation in Spintronics (CSIS), Core Research Cluster (CRC), Tohoku University, Sendai 980-8577, Japan* [6]*Center for Spintronics Research Network (CSRN), Tohoku University, Sendai 980-8577, Japan* [7]*Oarai Center, Institute of Material Research, Tohoku University, Oarai, Ibaraki, 311-1313, Japan*

Nowadays advanced magnetic tunnel junction applications demand very high tunnel magnetoresistance at room temperature, thus it is quite important to explore high Curie temperature T_c half-metallic Heusler alloys. In this article first-principles calculation unveiled that NiCrMnSi has T_c of 1200 K comparable to that of the traditional Co_2MnSi Heusler alloys, even though it does not contain Co element. In addition, we examined whether NiCrMnSi Heulser phase films can be obtained by a magnetron sputtering on MgO substrates. The results of the structural analysis and first-principles calculations indicated that NiCrMnSi Heusler phase is metastable. A possible route to obtain metastable NiCrMnSi Heusler alloy is to utilize appropriate templates.

1. Introduction

Magnetic tunnel junctions (MTJs) are currently being widely used for various commercial applications, such as storage, sensor, and memory. More recently, advanced computing technologies are emergent and demand MTJs exhibiting much higher tunnel magnetoresistance (TMR) ratio at room temperature.[1–3] Large TMR ratios can be obtained in MTJs with a use of electrodes of half-metallic ferromagnets which are magnetic metals having a band gap at the Fermi level for their minority spin state.[4] A Co_2-based Heusler alloy is one of the candidates of half-metals and attracted much attention to date.[5] Among several kinds of Co_2-based Heusler alloys, a promising one for

*E-mail: shigemi.mizukami.a7@tohoku.ac.jp

MTJs is Co_2MnSi.[6] Indeed, MTJs with electrodes of Co_2MnSi or of the ones with Mn partially substituted by Fe showed the record of the TMR ratio of about 2600% at low temperature.[7] However, this TMR ratio is significantly reduced at room temperature.[7] The reduction of the TMR ratio with elevating temperature is due to thermal fluctuation of a magnetic moment,[8–10] hence it can be suppressed with use of half-metals with higher Curie temperatures T_c.

A numerous elemental combinations in Heusler alloys enabled us to find new compositions showing unconventional electronic structures, such as a spin gapless semiconductor.[11] Furthermore, computation-based exploration are much progressed.[12–15] However, there are yet no computational reports focusing on half-metallic Heusler alloys with high T_c beyond those of Co_2MnSi and the derivatives.

As a first step of computational/experimental explorations for high T_c half-metallic Heusler alloys, we theoretically and experimentally studied NiCrMnSi equiatomic quaternary alloys in this article. The *ab-initio* calculations unveiled, for the first time, that the NiCrMnSi Heusler alloy has attractive properties; such as a small net magnetic moment due to the ferrimagnetic spin structure, high T_c, and large spin polarization, even though elemental compositions are different from Co_2-based Heusler alloys. We also examined whether film growth of NiCrMnSi is possible using a magnetron sputtering technique. The experiments indicated that NiCrMnSi films are decomposed into other alloys/compounds without crystallizing into Heusler phase. This phase separation observed in the experiments is explained with the formation energies for NiCrMnSi and the others, and indicating that NiCrMnSi Heusler phase is rather metastable. A possible route to obtain the Heusler phase film of NiCrMnSi is discussed.

2. First-principles calculations

Ab-initio calculation of NiCrMnSi has been performed using Vienna Ab Initio Simulation Package,[16] in combination with the projector augmented wave method.[17] For the exchange correlation potential, we used the generalized gradient approximation (GGA).[18] The energy cutoff of 500 eV has been set for the plane waves, and the final energies have been calculated with a k-mesh of $8 \times 8 \times 8$ for the cubic case and a comparable number of k-points used for the tetragonal case. The energy and the force tolerance were 10 μeV and 10 meV/Å, respectively.

Magnetic interactions and the detail insight of magnetism have been probed using Green's function based spin-polarized relativistic Korringa-Kohn-Rostoker method

Table I. Calculated formation energies $\Delta E_{\mathrm{XX'YZ}}$ and lattice constant a for cubic and tetragonal Ni-Cr-Mn-Si Heusler alloys with different types. c/a is the axial ratio of the tetragonal unit cell.

XX'YZ	structure	$\Delta E_{\mathrm{XX'YZ}}$ (eV/f.u.)	a (Å)	c/a
NiCrMnSi	cubic	-1.033	5.710	
	tetragonal	-1.151	5.285	1.270
MnNiCrSi	cubic	-0.974	5.681	
	tetragonal	-1.118	5.213	1.254
MnCrNiSi	cubic	-0.402	5.658	
	tetragonal	-0.794	5.046	1.457

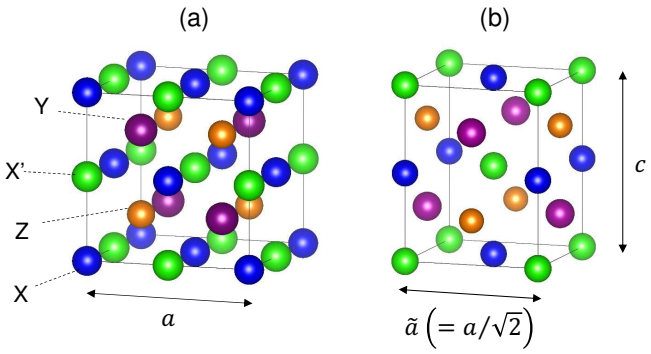

Fig. 1. Illustration of a crystal structure of Y ordered equiatomic Heusler alloy XX'YZ with (a) cubic ($a = c$) or (b) tetragonal ($a \neq c$) lattice. Cubic XX'YZ Heusler structure has a space group of $F\bar{4}3m$ (no. 216) and tetragonal lattice has a space group of $I\bar{4}m2$ (no. 119).

(SPR-KKR) as implemented in the programme package.[19] We calculate the Heisenberg exchange coupling constant within a real space approach as proposed by Liechenstein *et al.*[20] Furthermore, T_c has been calculated in terms of the Heisenberg exchange coupling constant, within mean field approximation. For the self-consistent-field calculations we use the full-potential method and GGA for the exchange correlation potential. We use 824 irreducible k-points for the Brillouin zone integration and an angular momentum expansion up to 3 has been used for each atom. 90 energy points on the complex energy path were used.

We evaluated the formation energy for the three types of ordered structure of NiCrMnSi with cubic or tetragonal structures, as shown in Fig. 1. Here the formation energy $\Delta E_{\mathrm{XX'YZ}}$ is defined as,

$$\Delta E_{\mathrm{XX'YZ}} = E_{\mathrm{XX'YZ}} - \left[E_{\mathrm{X}} + E_{\mathrm{X'}} + E_{\mathrm{Y}} + E_{\mathrm{Z}}\right], \tag{1}$$

where $E_{\mathrm{XX'YZ}}$ denotes the total energy of the Heusler alloy XX'YZ, and E_{X}, $E_{\mathrm{X'}}$, E_{Y}

Table II. Physical properties of tetragonal NiCrMnSi predicted from the first principles; the Curie temperature T_c, the spin polarization P, the basal plane lattice constant a, the axial ratio c/a, and the total magnetic moment $m_{\rm tot}$. The values for Co_2MnSi similarly calculated from the first principles are also shown for comparison. Values in the parentheses correspond to the partial magnetic moments of Ni, Cr, and Mn atom for NiCrMnSi and those of Co and Mn atom for Co_2MnSi, respectively.

Material	T_c (K)	P (%)	a (nm)	c/a	$m_{\rm tot}$ (μ_B/f.u.)
NiCrMnSi	1200	88	0.528	1.27	0.95 (0.13, −1.79, 2.61)
Co_2MnSi	1204	100	0.563	1.00	5.00 (1.02, 2.99)

and $E_{\rm Z}$ are those of elemental solids, X, X', Y and Z, respectively. Then we found the tetragonal type of NiCrMnSi is the most stable in terms of the formation energy, as shown in Table I. The predicted physical properties are summarized in Table II. We also calculated the values for Co_2MnSi from the first principles and those are also shown in the Table II for comparison. The Curie temperature of NiCrMnSi is as high as that of Co_2MnSi, which stems from the large antiferromagnetic exchange interaction between magnetic moments for Cr and Mn. Note that the mean-field approximation usually tends to overestimate the Curie temperature since it neglects the thermal fluctuation of magnetic moments. Indeed, the Curie temperature experimentally observed for Co_2MnSi was 990 K.[21] Total magnetic moment is close to 1 μ_B and the spin polarization is close to unity, because the Fermi level is located near the top of the valence band edge for the minority spin state, as shown in Fig. 2(a). Importantly, the Δ_1 band dispersion along the [001] axis is located across the Fermi level for the majority spin state and no Δ_1 bands are located at the Fermi level for the minority spin state, as shown in Figs. 2(b) and 2(c), respectively. This means that the Δ_1 band which determines the TMR ratio in MgO-based MTJs is fully spin polarized, hence the large TMR ratio is expected, as theoretically predicted and experimentally observed in bcc Fe(-Co)/MgO MTJs.[22–26]

3. Experiments

3.1 Experimental procedures

All samples were prepared by a magnetron sputtering system with a base pressure of 2×10^{-7} Pa, as previously used in different Heusler alloy films.[27–30] The single crystal MgO(001) substrates were cleaned by ultrasonic cleaning in an acetone and an ethanol prior to being introducing into the load-lock chamber. Sample stacking structure was

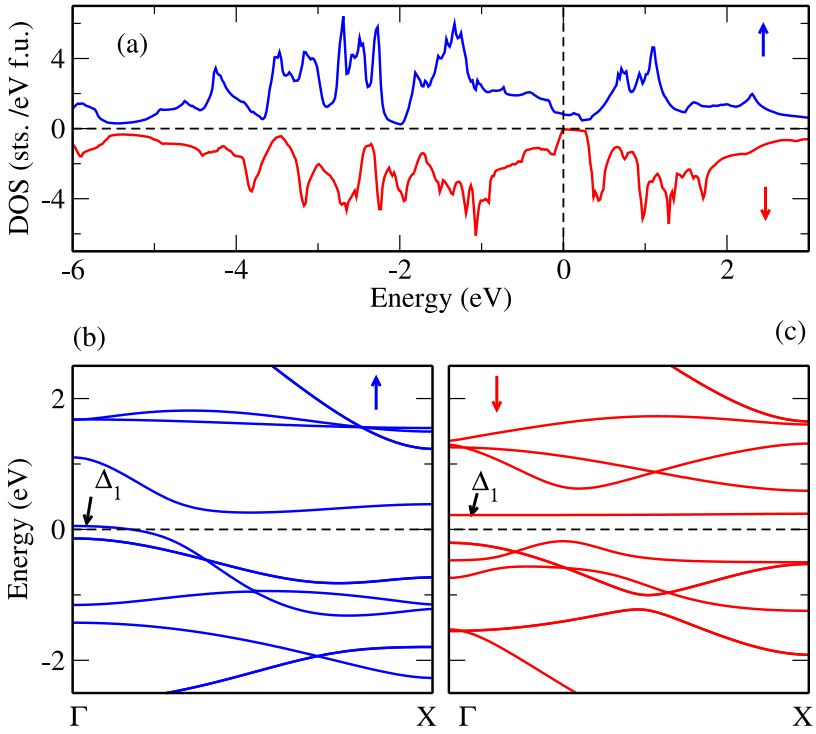

Fig. 2. Electronic structure calculated from the first principles for a tetragonal NiCrMnSi. (a) The density-of-states, and the band dispersion along the [001] axis for (b) majority and (c) minority spin states.

MgO(001) substrate /NiCrMnSi(100 nm)/Ta(3 nm). The substrates were thermally flushed at 700°C in the chamber to remove residual organic substances and water. NiCrMnSi layers were deposited by a co-sputtering technique using NiCr and MnSi alloy targets. Powers were 100 W, 30 W, 26 W and 60 W in the Cr, NiCr, MnSi and Ta targets, respectively. The composition of Ni : Cr : Mn : Si in the films was evaluated as 25.9 : 29.5 : 23.0 : 21.6 (at%) by an inductively coupled plasma mass spectrometry (ICP-MS). The 100-nm-thick NiCrMnSi layers were deposited at a substrate temperature T_s of 500–800°C. Finally, Ta capping layers were deposited at room temperature. The crystalline structure of the samples was measured by an out-of-plane X-ray diffraction (XRD) with Cu K_α radiation (wavelength of 0.15418 nm) and a transmission electron microscope (TEM). Magnetic property was measured using a polar magneto-optical Kerr effect (p-MOKE) with a maximum magnetic field of 2 T and a laser wavelength of approximately 400 nm. Magnetization measurements were also carried out using a vibrating sample magnetometer (VSM) with a maximum in-plane magnetic field of 2

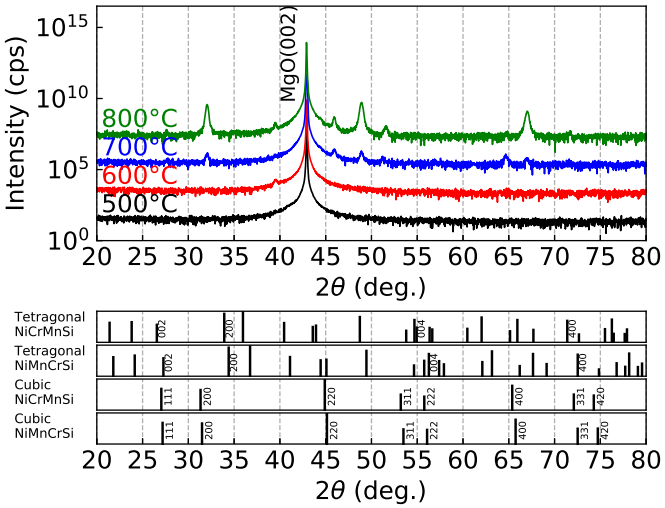

Fig. 3. Out of plane XRD patterns of NiCrMnSi films with different deposition temperatures. Theoretical diffraction patterns for the NiCrMnSi and NiMnCrSi Heusler phases with cubic and tetragonal structures are shown at the bottom.

T.

3.2 Experimental results

The out-of-plane XRD patterns for the NiCrMnSi films on MgO substrates with different deposition temperatures are shown in Fig. 3. The powder diffraction patterns for the NiCrMnSi Heusler phase with cubic and tetragonal structures are theoretically simulated and are also plotted at the bottom for comparison. The diffraction peaks were observed for the samples with $T_s \geq 700$°C and the peak intensity increased with increasing the annealing temperature. However, the peak positions were not consistent with those from the cubic or tetragonal phase. Therefore, the other phases might be formed in these samples. However, there are many candidates consisting each element corresponding to these peaks and it is difficult to identify the formed phases from these XRD patterns.

To consider the phase formed in these samples, TEM observation was performed. Figures 4(a) and 4(b) show the TEM images for NiCrMnSi films deposited on MgO substrates at 500°C with low and high magnification, respectively. Figures 4(c) and 4(d) similarly show those for the films deposited at 700°C with low and high magnification, respectively. The corresponding diffraction patterns are included as insets in these figures. In the case for the sample deposited at 500°C, some short-range crystallization phases were observed and the ring pattern for the diffraction images indicated

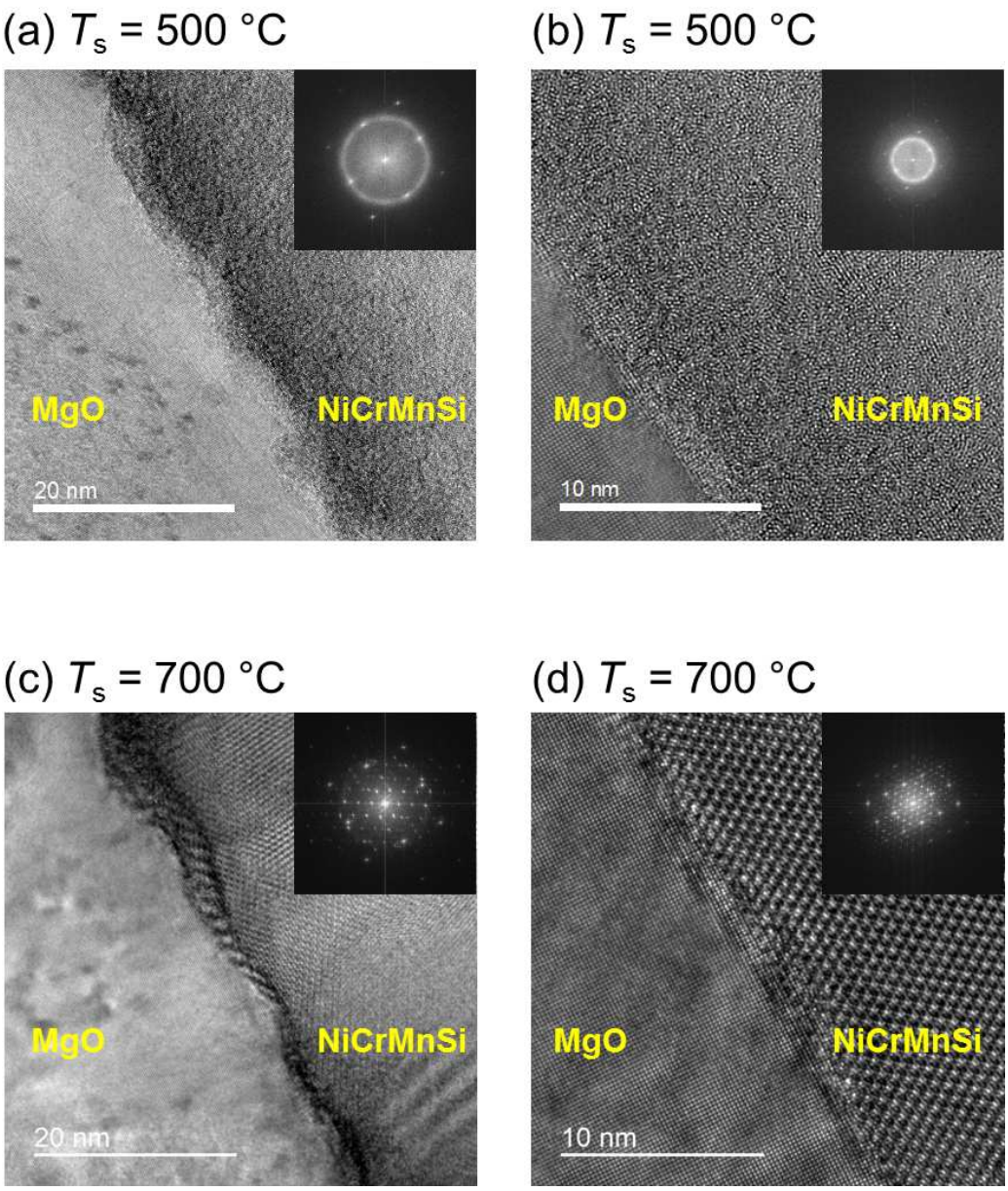

Fig. 4. TEM images of NiCrMnSi deposited at 500°C and 700°C. (a) Low and (b) high magnification images for NiCrMnSi deposited at 500°C. (c) Low and (d) high magnification images for NiCrMnSi deposited at 700°C. Insets are the corresponding selected beam electron diffraction pattern.

the formation of polycrystalline. Because of the short-range crystallization, XRD measurements showed no diffraction peak in Fig. 3. On the other hand, in the case for the sample deposited at 700°C, the grain boundaries are observed clearly for the images with low magnification. It suggested the grain sizes are larger than those for the sample deposited at 500°C. Furthermore, the diffraction spots were observed and suggested

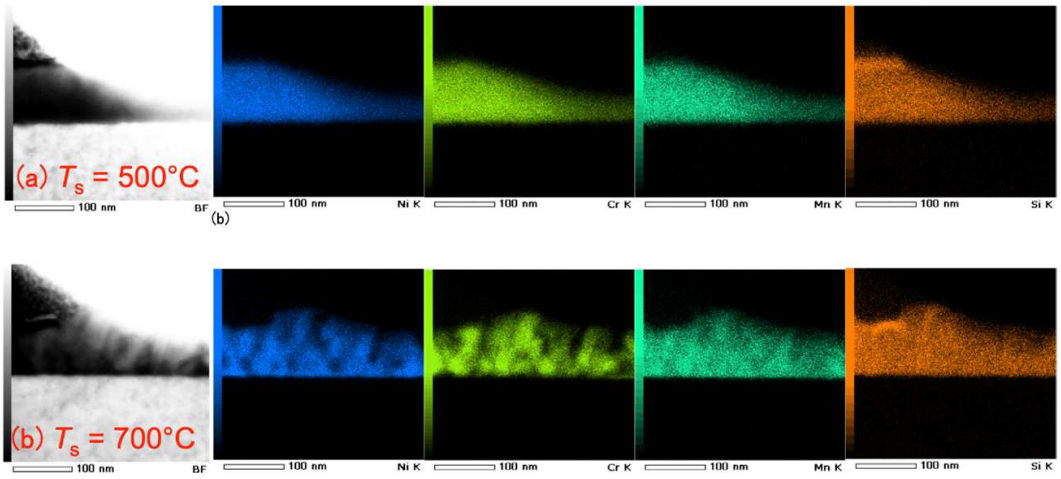

Fig. 5. Element mapping images by TEM-EDX for NiCrMnSi samples deposited at (a) 500°C and (b) 700°C. Left images are TEM images. Blue, yellow green, and orange data points corresponding to the Ni, Cr, Mn and Si elements, respectively.

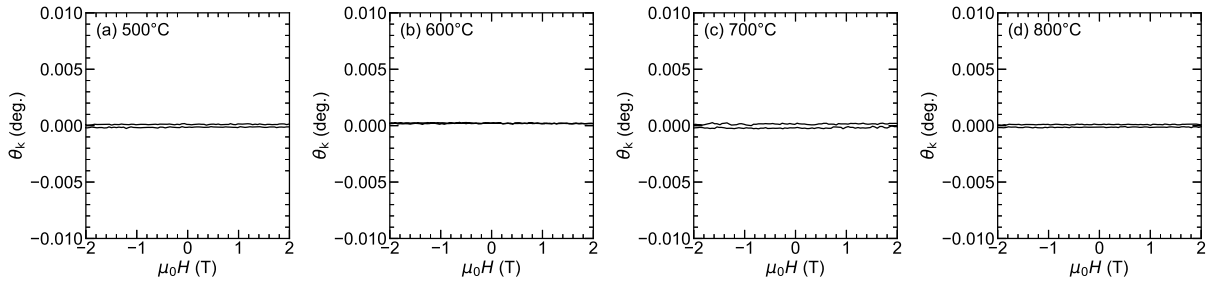

Fig. 6. p-MOKE results for the NiCrMnSi deposited at (a) 500°C, (b) 600°C, (c) 700°C, and (d) 800°C.

that multiple crystalline phases were formed as seen as their overlapped patterns. Observation agrees with the fact that many diffraction peaks were observed in the XRD measurements for the sample deposited at 700°C in Fig. 3.

For further analysis, the elemental mapping was performed by energy dispersive X-ray spectrometry (EDX) in the TEM apparatus. Figures 5(a) and 5(b) show the cross-sectional TEM images and elemental mapping images for NiCrMnSi films deposited at 500°C and 700°C, respectively. Left figures are cross-sectional TEM images and the other four figures are elemental mapping images. Blue, yellow-green, green, and orange correspond to the detected Ni, Cr, Mn, and Si elements, respectively. For the sample deposited at 500°C, all four elements were homogeneously distributed in a whole region. However, non-uniform distributions for Ni and Cr atoms were observed and these are complementary for the sample deposited at 700°C. It suggests that the Ni-rich phase

and the Cr-rich phase were spatially separated in this sample.

The magnetic properties of NiCrMnSi films were measured by using the p-MOKE. Figure 6 shows the out-of-plane MOKE curves for the NiCrMnSi films with different deposition temperatures. No hysteresis loop was observed for all the samples even at the deposition temperature of 800°C. Some samples were also measured using VSM, however, no hysteresis loop was observed. These results suggested that all samples in this study showed paramagnetism or antiferromagnetism at room temperature.

4. Discussion

To investigate which phases were formed, the out-of-plane XRD pattern with the wide range from 10° to 90° for the sample deposited at 800°C is shown in Fig. 7(a). From the XRD analysis and TEM observation, (001)-orientated $Mn_6Ni_{16}Si_7$ and Mn_3Si may be formed as dominants phases in the samples. Figures 7(b) and 7(c) show the crystalline lattices of $Mn_6Ni_{16}Si_7$ and Mn_3Si, respectively. $Mn_6Ni_{16}Si_7$ and Mn_3Si are antiferromagnets with the Neel temperatures of $\simeq$200 K[31] and 23 K,[32] respectively. Therefore, this analysis is consistent with the magnetic measurements which showed no hysteresis loop in Fig. 6. In addition to the above mentioned phases, there exist minor phases. For example, some peaks as appeared in Fig. 3 and Fig. 7(a) cannot be attributed to $Mn_6Ni_{16}Si_7$, and Mn_3Si. Those unknown phases may be Cr-rich alloys or compounds and minor residues.

The phase stability can be discussed by the difference δE in the formation energy of NiCrMnSi and alloys/compounds decomposed. When we assume that the above-mentioned unknown phases are Cr_3Si and Si, δE is evaluated as,

$$\begin{aligned} \delta E &= \Delta E_{\mathrm{NiCrMnSi}} \\ &- \left[\frac{1}{16}\Delta E_{\mathrm{Mn_6Ni_{16}Si_7}} + \frac{5}{24}\Delta E_{\mathrm{Mn_3Si}} + \frac{1}{3}\Delta E_{\mathrm{Cr_3Si}} + \frac{1}{48}\Delta E_{\mathrm{Si}}\right]. \end{aligned}$$

Here, $\Delta E_{\mathrm{Mn_6Ni_{16}Si_7}}$, $\Delta E_{\mathrm{Mn_3Si}}$, $\Delta E_{\mathrm{Cr_3Si}}$, and ΔE_{Si} are the formation energies of bulk $Mn_6Ni_{16}Si_7$, Mn_3Si, Cr_3Si, and Si, respectively which are found to be -12.686 eV/f.u., -1.334 eV/f.u., -1.436 eV/f.u., and 0 eV/f.u. After substituting these values in the above equation, we obtain $\delta E = 0.396$ eV/f.u. The positive value of δE means that the Heusler phase of NiCrMnSi is not stable at ground state and tends to be decomposed into the others in the bulk form. Thus this analysis reasonably accounts the experimental observations.

Above discussion implies that the Heusler phase of NiCrMnSi is rather metastable.

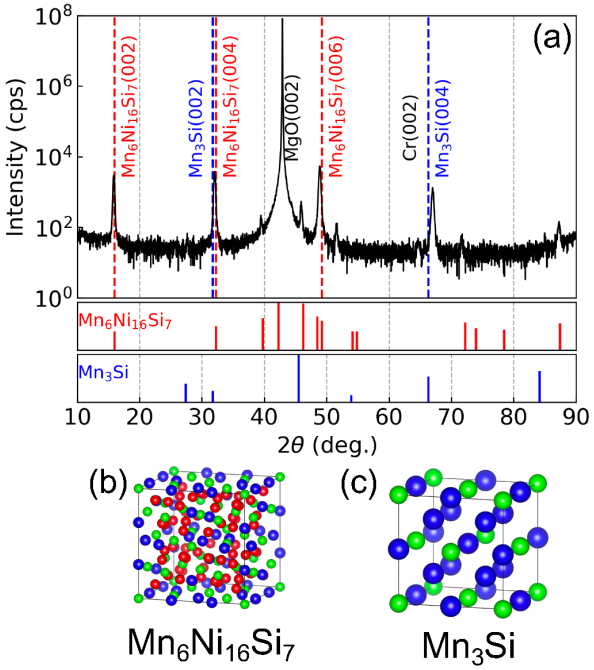

Fig. 7. (a) Wide range out of plane XRD pattern of NiCrMnSi deposited at 800°C. Theoretical diffraction patterns for $Mn_6Ni_{16}Si_7$ and Mn_3Si are shown at the bottom. Cartoons of the crystal lattice of (b) $Mn_6Ni_{16}Si_7$ and (c) Mn_3Si.

In general, metastable phases of alloy films can be obtained when those are grown on an appropriate template with optimized growth conditions such as film thickness and growth temperatures. In particular, relatively low temperature growth on a specific alloy template would be effective, as well known in tetragonal Mn-based Heusler alloys and those derivatives, for example.[33–40] Thus, it would be crucial to find good templates for obtaining the Heusler phase of NiCrMnSi, which is left as a future subject.

5. Summary

We theoretically and experimentally studied on NiCrMnSi equiatomic Heusler alloys. The first principles calculation predicted that the tetragonal NiCrMnSi was energetically favorable compared with the cubic phase and possessed the high Curie temperature and the fully spin-polarized electronic band along [001] directions. NiCrMnSi equiatomic alloy films were fabricated by magnetron sputtering. The XRD measurements indicated that several phases were formed for the samples deposited at high deposition temperatures. The TEM observation showed that the Ni-rich and Cr-rich phases were spatially separated in those films. The p-MOKE and VSM measurements showed no magnetic hysteresis loop, which suggested that all samples have paramagnetism or antiferromag-

netism at room temperature. This phase separation was also theoretically explained in terms of the formation energies of NiCrMnSi and the other decomposed alloys and compounds. A possible route to obtain the NiCrMnSi single phase Heusler alloys as the metastable phase is to utilize more appropriate template to promote the crystallization of NiCrMnSi Heusler alloys at relatively lower temperature.

acknowledgement

This work was partially supported by JST CREST (No. JPMJCR17J5).

References

1) A. Sengupta and K. Roy, IEEE Trans. Circuits Syst. **63,** 2267 (2016).
2) Z. Chowdhury, J.D. Harms, S.K. Khatamifard, M. Zabihi, Y. Lv, A.P. Lyle, S.S. Sapatnekar, U.R. Karpuzcu, and J.-P. Wang, IEEE Comput. Archit. Lett. **17,** 42 (2018).
3) M. Zabihi, Z.I. Chowdhury, Z. Zhao, U.R. Karpuzcu, J.-P. Wang, and S.S. Sapatnekar, IEEE Trans. Comput. **68,** 1159 (2019).
4) W. E. Pickett and J. S. Moodera, Phys. Today, **54,** 39, (2001).
5) I. Galanakis, P.H. Dederichs, and N. Papanikolaou, Phys. Rev. B **66,** 174429 (2002).
6) Y. Sakuraba, M. Hattori, M. Oogane, Y. Ando, H. Kato, A. Sakuma, T. Miyazaki, and H. Kubota, Appl. Phys. Lett. **88,** 10 (2006).
7) H. Liu, T. Kawami, K. Moges, T. Uemura, M. Yamamoto, F. Shi, and P.M. Voyles, J. Phys. D. Appl. Phys. **48,** 164001 (2015).
8) S. Zhang, P.M. Levy, A.C. Marley, and S.S.P. Parkin, Phys. Rev. Lett. **79,** 3744 (1997).
9) C.H. Shang, J. Nowak, R. Jansen, and J.S. Moodera, Phys. Rev. B **58,** 2917(R) (1998).
10) B. Hu, K. Moges, Y. Honda, H. Liu, T. Uemura, M. Yamamoto, J. Inoue, and M. Shirai, Phys. Rev. B **94,** 094428 (2016).
11) G. Z. Xu et al., EPL (Europhysics Lett.), **102,** 17007 (2013).
12) A.O. Oliynyk, E. Antono, T.D. Sparks, L. Ghadbeigi, M.W. Gaultois, B. Meredig, and A. Mar, Chem. Mater. **28,** 7324 (2016).
13) F. Legrain, J. Carrete, A. van Roekeghem, G.K.H. Madsen, and N. Mingo, J. Phys. Chem. B **122,** 625 (2018).
14) X. Zheng, P. Zheng, and R.-Z. Zhang, Chem. Sci. **9,** 8426 (2018).
15) K. Kim, L. Ward, J. He, A. Krishna, A. Agrawal, and C. Wolverton, Phys. Rev. Mater. **2,** 123801 (2018).
16) G. Kresse, J. Furthm 端 ller, Phys. Rev. B, 54 (1996) 11169; G. Kresse, D. Joubert, Phys. Rev. B, **59,** 1758 (1999).
17) P.E. Bloechl, Phys. Rev. B **50,** 17953 (1994).
18) J.P. Perdew, K. Burke, M. Ernzerhof, Phys. Rev. Lett. **77,** 3865 (1996).
19) The Munich SPR-KKR package, Version 6.3, H. Ebert etal;http://olymp.cup.uni-

muenchen.de/ak/ebert/SPRKKR; Rep. Prog. Phys. **59,** 1665 (1996).
20) A.I. Liechtenstein, M.I. Katsnelson, V.P. Antropov, V.A. Gubanov, J. Magn. Magn. Mater. **67,** 65 (1987).
21) K. H. J. Buschow and P. G. van Engen, J. Magn. Magn. Mater. **25,** 90 (1981).
22) W.H. Butler, X.-G. Zhang, T.C. Schulthess, and J.M. MacLaren, Phys. Rev. B **63,** 054416 (2001).
23) J. Mathon and A. Umerski, Phys. Rev. B **63,** 220403 (2001).
24) J. Faure-Vincent, C. Tiusan, E. Jouguelet, F. Canet, M. Sajieddine, C. Bellouard, E. Popova, M. Hehn, F. Montaigne, and A. Schuhl, Appl. Phys. Lett. **82,** 4507 (2003).
25) S. Yuasa, T. Nagahama, A. Fukushima, Y. Suzuki, and K. Ando, Nat. Mater. **3,** 868 (2004).
26) S.S.P. Parkin, C. Kaiser, A. Panchula, P.M. Rice, B. Hughes, M. Samant, and S.-H. Yang, Nat. Mater. **3,** 862 (2004).
27) L. Bainsla, R. Yilgin, J. Okabayashi, A. Ono, K. Suzuki, and S. Mizukami, Phys. Rev. B, **96,** 094404, (2017).
28) L. Bainsla, K.Z. Suzuki, M. Tsujikawa, H. Tsuchiura, M. Shirai, and S. Mizukami, Appl. Phys. Lett. **112,** 052403 (2018).
29) L. Bainsla, R. Yilgin, M. Tsujikawa, K. Z. Suzuki, M. Shirai, and S. Mizukami, J. Phys. D. Appl. Phys., **51,** 495001, (2018).
30) T. Tsuchiya, T. Roy, K. Elphick, J. Okabayashi, L. Bainsla, T. Ichinose, K.Z. Suzuki, M. Tsujikawa, M. Shirai, A. Hirohata, and S. Mizukami, Phys. Rev. Mater. **3,** 084403 (2019).
31) S. J. Ahmed, J. E. Greedan, C. Boyer, and M. Niewczas, Inorg. Chem., **57,** 14144 (2018).
32) C. Pfleiderer, J. Boeuf, and H. v. Loehneysen, Phys. Rev. B, **65,** 172404 (2002).
33) K.Z. Suzuki, R. Ranjbar, A. Sugihara, T. Miyazaki, and S. Mizukami, Jpn. J. Appl. Phys. **55**, 010305(R) (2016).
34) K.Z. Suzuki, R. Ranjbar, J. Okabayashi, Y. Miura, A. Sugihara, H. Tsuchiura, and S. Mizukami, Sci. Rep. **6,** 30249 (2016).
35) K.Z. Suzuki, Y. Miura, R. Ranjbar, L. Bainsla, A. Ono, Y. Sasaki, and S. Mizukami, Appl. Phys. Lett. **112,** 062402 (2018).
36) P.C. Filippou, J. Jeong, Y. Ferrante, S.-H. Yang, T. Topuria, M.G. Samant, and S.S.P. Parkin, Nat. Commun. **9,** 4653 (2018).

37) K. Kunimatsu, K. Z. Suzuki, and S. Mizukami, J. Cryst. Growth, **514,** 8 (2019).
38) M. Yamanouchi, N. V. Bao, M. Inoue, and T. Uemura, Jpn. J. Appl. Phys., **58,** 100903, (2019).
39) D. Oshima, T. Kato, and S. Iwata, AIP Adv., **10,** 025012 (2020).
40) A. Nogueron, H. N. Fern叩ndez-Escamilla, J. Guerrero-S叩nchez, and N. Takeuchi, Appl. Surf. Sci., **504,** 144332 (2020).